ADVANCED MATERIALS
www.advmat.de

Motion-Adaptive Tessellated Skin Patches With Switchable Adhesion for Wearable Electronics

Geonjun Choi, Jaeil Kim, Hyunjoong Kim, Haejin Bae, Baek-Jun Kim, Hee Jin Lee, Hyejin Jang, Minho Seong, Salah M. Tawfik, Jae Joon Kim, and Hoon Eui Jeong**

Skin-interfaced electronics have emerged as a promising frontier in personalized healthcare. However, existing skin-interfaced patches often struggle to simultaneously achieve robust skin adhesion, adaptability to dynamic body motions, seamless integration of bulky devices, and on-demand, damage-free detachment. Here, a hybrid strategy that synergistically combines these critical features within a thin, flexible patch platform is introduced. This design leverages shape memory polymers (SMPs) arranged in a tessellated array, comprising both rigid and compliant SMPs. This configuration enables exceptional deformability, motion adaptability, and ultra-strong, repeatable skin adhesion while offering on-demand adhesion control. Furthermore, the design facilitates the seamless integration of bulky electronics without compromising skin adhesion. By incorporating sizeable electronics including signal acquisition circuits, sensors, and a battery, it is demonstrated that the proposed tessellated patch can be securely mounted on the skin, accommodate dynamic body motions, precisely detect physiological signals with an outstanding signal-to-noise ratio (SNR), wirelessly transmit data, and be effortlessly released from the skin.

1. Introduction

Skin-interfaced electronics (SIEs) represent a rapidly evolving class of bioelectronic devices that integrates seamlessly with human skin, enabling continuous monitoring of diverse physiological signals.[1] These devices are poised to transform various fields, from personalized health monitoring[2] and transdermal drug delivery[3] to human-machine interactions.[4] A critical challenge in realizing the full potential of SIEs is achieving robust and intimate adhesion with the skin, which is essential for both user comfort and high-quality biometric signal acquisition.[5] Inadequate adhesion can lead to signal degradation and increased motion artifacts, significantly compromising device reliability.[6]

Beyond achieving stable skin adhesion under static conditions, these devices must also adapt to dynamic movements.[7] Users of SIEs engage in a variety of activities, subjecting the devices to significant strain. Therefore, the devices need to be both skin-conformable and motion-adaptable. However, maintaining close contact under both static and dynamic conditions is challenging because skin is a complex surface with considerable roughness and dynamic properties.[8] Traditional approaches have relied on chemical adhesives, which often result in skin irritation, particularly in vulnerable infants and the elderly.[9] Additionally, environmental factors like temperature and sweat can undermine long-term adhesion stability.[10]

In response to these challenges, epidermal electronics have emerged as a promising solution.[11] These ultra-thin electronics can conform to the skin's topography with minimal chemical adhesives.[12] This approach enhances the signal quality while mitigating skin damage. Additionally, their high compliance improves motion adaptability.[13] Despite these advantages, epidermal electronics typically exhibit weak skin adhesion primarily relying on van der Waals interactions.[14] This weak adhesion limits the integration of bulky electronic components such as wireless communication modules and batteries. Consequently, many epidermal devices rely on near-field communication, which restricts their operational range.[9a] Furthermore, their extreme thinness poses challenges in device handling, durability, and reusability.[9b]

G. Choi, J. Kim, H. J. Lee, H. Jang, S. M. Tawfik, H. E. Jeong
Department of Mechanical Engineering
Ulsan National Institute of Science and Technology (UNIST)
Ulsan 44919, Republic of Korea
E-mail: hoonejeong@unist.ac.kr

H. Kim, J. J. Kim
Department of Electrical Engineering
Ulsan National Institute of Science and Technology (UNIST)
Ulsan 44919, Republic of Korea
E-mail: jaejoon@unist.ac.kr

H. Bae, B.-J. Kim
Ecological Technology Team, Division of Ecological Application Research
National Institute of Ecology
Seocheon 33657, Republic of Korea

M. Seong
Department of Fire Protection Engineering
Pukyong National University
Busan 48513, Republic of Korea

The ORCID identification number(s) for the author(s) of this article can be found under https://doi.org/10.1002/adma.202412271

DOI: 10.1002/adma.202412271

SMPs have emerged as another potential solution to these adhesive challenges in wearable electronics.[15] For a given adhesion energy (G_c), the adhesion force ($F \propto \sqrt{\frac{G_c A}{C}}$) is proportional to the square root of the true contact area (A) and inversely proportional to the compliance (C) of the adhesive system.[16] This indicates that the adhesion can be improved by maximizing the contact area and increasing material rigidity. SMPs can dynamically adjust their contact geometry and rigidity, enabling control over adhesion in response to thermal stimuli. However, their high rigidity at room temperature can restrict movements and even lead to delamination from the skin during motion, limiting their use in SIEs.[17] Despite recent advancements in wearable electronics, achieving a skin-interfaced patch that combines strong skin adhesion, motion adaptability, integration of bulky devices, and on-demand, damage-free detachment remains a challenge in the field.

Herein, we present a multifunctional skin adhesive patch that leverages material and structural hybrid heterogeneity in a thin film platform. The patch integrates discrete rigid and compliant SMP elements arranged in a tessellated array. This design simultaneously achieves impressive pull-off strength (1070.2 kPa), peel adhesion (200.9 N m^{-1}), a remarkable adhesion switching ratio (47.7), high reusability (>500 cycles), and excellent mechanical deformability with a low effective modulus (218.8 kPa). Additionally, the patch demonstrates low contact resistance (R_c) (38.8 kΩ μm), low skin contact impedance (44.1 kΩ at 10 Hz), and high SNR (22.5 dB). This multifunctionality allows for the seamless integration of bulky electronic components without compromising skin adhesion, enabling precise wireless detection of various physiological signals.

2. Results and Discussion

2.1. Design of the Motion-Adaptive Tessellated Skin Patch

The motion-adaptive tessellated skin patch (TSP) features a bioinspired design that integrates the surface adaptability of barnacles with the deformability of armadillos (**Figure 1a**). Barnacles are renowned for their ability to adhere to diverse surfaces, from smooth ship hulls to rough rocks (Figure 1a-i). This adhesion is achieved through barnacle cement, a polyprotein complex that forms a tight bond with the substrate and then hardens, providing excellent adhesion.[18] We replicated this capability using SMP nanocomposites.

Similar to barnacles, our SMP nanocomposite can achieve strong adhesion to rough surfaces by conforming at elevated temperatures and then stiffening upon cooling. However, the high stiffness of SMPs in the cooling state limits the mechanical flexibility. To overcome this, we drew inspiration from the armadillo carapaces, which features a tessellated structure balancing rigidity and flexibility. The armadillo's integument consists of rigid mineralized segments connected by compliant collagen fibrils (Sharpey's fibers), providing flexibility while maintaining stiffness (Figure 1a-ii).[19]

To incorporate these functionalities, we arranged rigid SMP and soft SMP elements in a periodic 2D array within a thin film (Figure 1b). The tessellated design interconnects rigid SMP segments with flexible SMP segments. The SMP nanocomposite is composed of stearyl acrylate (SA) and lauryl methacrylate (LMA) polymers cross-linked with ethylene glycol dimethacrylate (EGDMA), reinforced with silica nanoparticles (SNPs) for enhanced shape recovery (Figure 1c; Note S1 and Figures S1 and S2, Supporting Information for detailed material and chemical analyses). The rigidity of the SMP segments was controlled by varying the SA/LMA ratio and SNP content (Figures S3 and S4, Supporting Information).

When heated above its melting temperature (T_m), the SMP nanocomposite, including both rigid and compliant SMPs, behaves like rubber due to the amorphous alkyl side chains (Figure 1d-i,ii), allowing it to conform to rough surfaces (Figure S5, Supporting Information). Upon cooling below T_m, the SMP transitions into a rigid semicrystalline state as the side chains crystallize, increasing stiffness (Figure 1d-iii). This locks the conformed contact geometry and enhances interfacial adhesion ("on" state) at room temperature. When reheated above T_m, the SMP returns to its rubbery state and recovers its original shape due to its shape memory properties, reducing adhesion ("off" state).[20] Compared to other thermo-responsive materials like hydrogels, SMPs offer superior environmental stability, mechanical durability, and higher adhesion (see Note S1, Supporting Information for more details).[21]

For wearable electronics applications, we integrated silver nanowires (AgNWs) into the TSP to function as active sensing elements or electrodes (Figure 1b). AgNWs were selected for their flexibility, conductivity, and ease of processing.[22] The heterogeneous design of the TSP provides several key advantages over conventional homogeneous skin patches (non-tessellated skin patches, NSPs), such as enhanced motion adaptability, switchable adhesion, and versatile device integration (Figures 1e and S6; see Note S1 and Table S1, Supporting Information for more details).[23]

2.2. Thermomechanical and Surface Adaptive Behavior

Figure 2a presents the fabricated TSP, produced using a screen-printing technique with SMP (Figure S7, Supporting Information). At room temperature (30 °C), the patch features a periodic 2D array of opaque rigid islands and transparent compliant grids, with a film thickness of 200 μm. The opaque segments, measuring 2 mm wide (l_r), correspond to the rigid SMP, while the transparent segments, 1 mm wide (l_c), represent the compliant SMP (Figure S8, Supporting Information). The rigid and compliant segments exhibited a strong interfacial bonding strength of 1210 N m^{-1}, confirming the TSP's mechanical robustness (Figure 2a-ii). SNPs with an average diameter of 200 nm were uniformly embedded in the SMP composite (Figure 2a-iii).

The mechanical properties of the TSP were adjusted by varying the LMA-to-SA weight ratio in the rigid and compliant segments (Figure S3, Supporting Information). The rigid segment, with a 7:3 SA:LMA ratio, displayed a storage modulus (G') of 36.9 MPa, while the compliant segment, with a 3:7 ratio, exhibited a G' of 136 kPa at room temperature. This composition created a distinct rigid-compliant mechanical heterogeneity within the TSP (Figure 2b-i). Upon heating above 45 °C, both segments transitioned to a rubbery state, with significantly reduced G' values of 118.9 and 107.6 kPa, respectively (Figure 2b-ii,iii). This

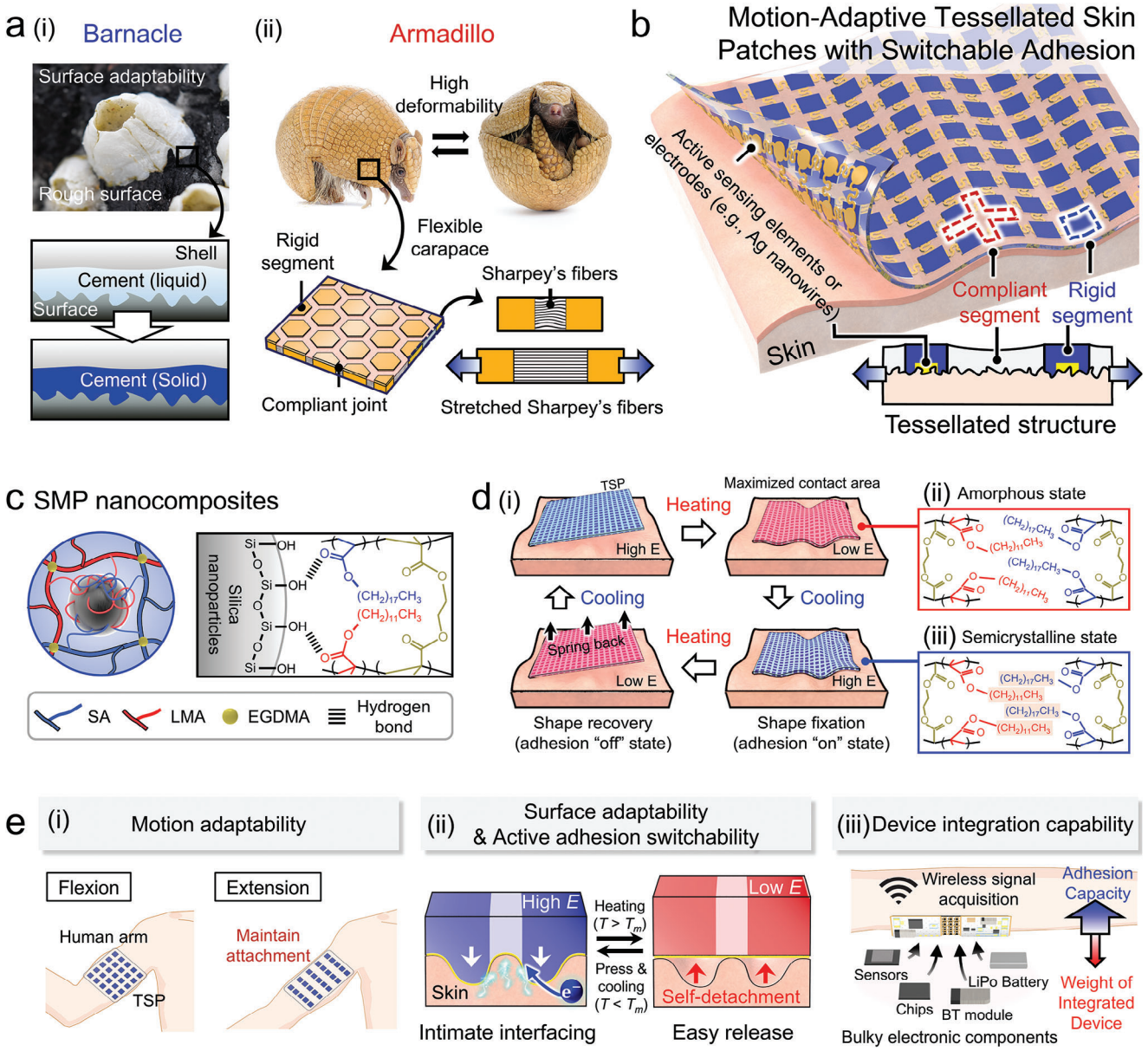

Figure 1. Design of motion-adaptive tessellated skin patches. a) Schematics illustrating i) the surface adaptability of barnacles on rough surfaces and ii) the high deformability of armadillos. The photographs of the barnacle and armadillo are used with permission and licensed from Adobe Stock (Photos by KerryDez Photography and Eastman Arts). b) Schematic of the TSP conformally attached to dynamic skin substrates, showing its tessellated structures with rigid and compliant segments, integrated with active sensing elements or electrodes. c) Chemical structure of SMP nanocomposites with SNP reinforcement. d) i) Adhesion mechanism of the SMP nanocomposite on rough skin surfaces, and chemical structures of ii) amorphous side chains at elevated temperature and iii) semicrystalline side chains at room temperature. e) Key advantages of the TSP: i) motion adaptability, ii) switchable active adhesion, and iii) versatile device integration capability.

behavior allows the TSP to conform effectively to rough skin surfaces at elevated temperatures while maintaining strong adhesion and motion-adaptive deformability at room temperature. The transition between states occurs in less than 12.5 s (Figure S9, Supporting Information). In contrast, the NSP displayed uniformly high stiffness (G' of 36.9 MPa) at room temperature, limiting its flexibility (Figure 2b-iv).

Optimizing the T_m of the TSP is crucial for wearable applications. Ideally, the TSP should maintain its rigid semicrystalline state for robust adhesion at body temperature (36.5–37.5 °C) while being capable of transitioning to a rubbery state for skin adaptation at elevated temperatures below the thermal injury threshold (45 °C). Previous research shows thermal damage can be avoided at 45 °C for up to 150 min, but risks increase quickly at higher temperatures (e.g., 47 °C causes damage within 35 min, and 50 °C within 1 min).[24] A 7:3 SA:LMA ratio achieved an optimal T_m of 43 °C (Figure 2c). Increasing the SA ratio raised the T_m because the longer alkyl chain of SA compared to LMA leads

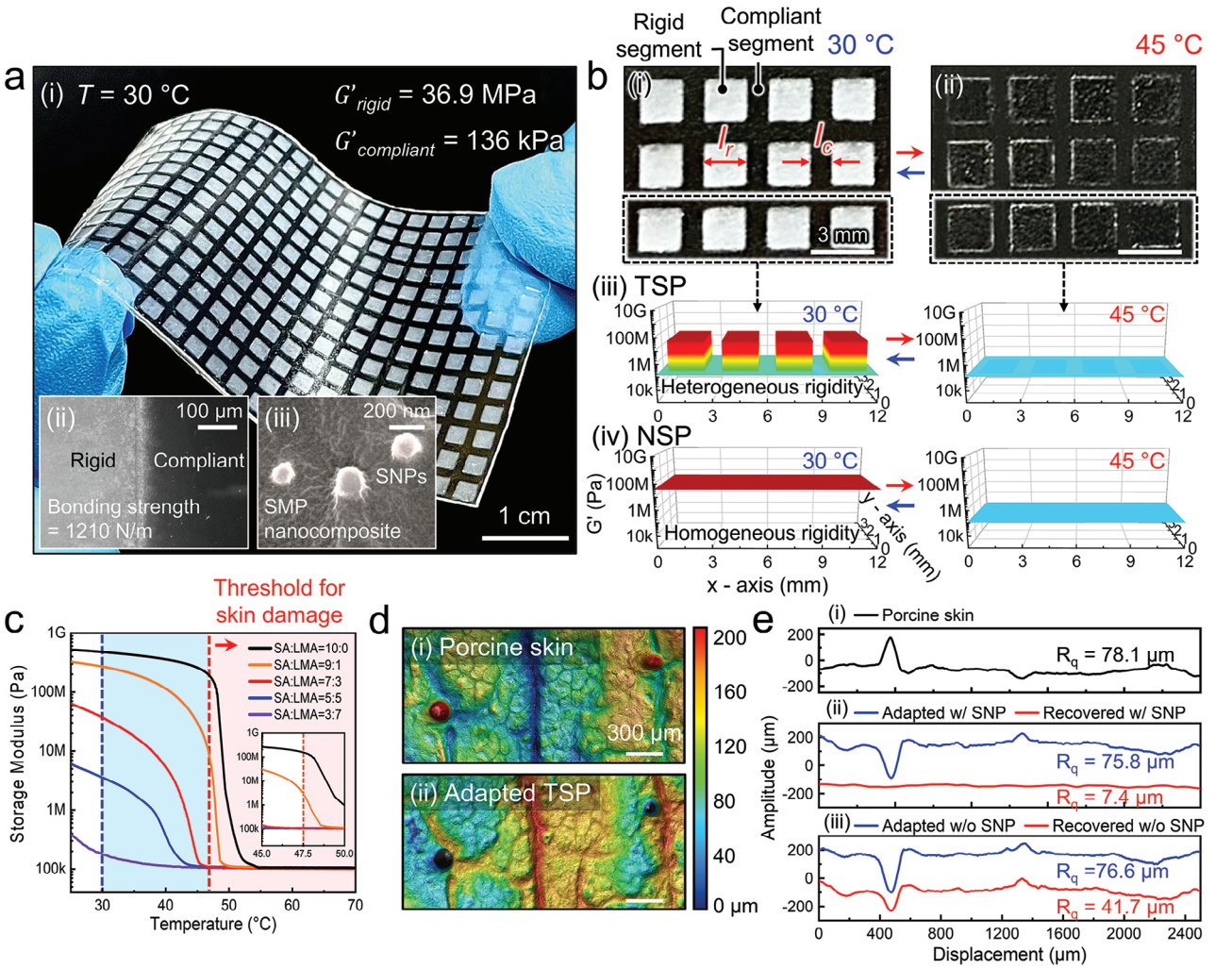

Figure 2. Thermomechanical and surface-adaptive behavior of the TSP. a) i) Photograph of the fabricated TSP. Insets show ii) an optical microscopy image of the bonding interface between the rigid and compliant segments, and iii) a cross-sectional SEM image of the SNP-reinforced SMP composite. b) Top-view photographs of the TSP at i) 30 °C and ii) 45 °C. Storage modulus (G') profiles of iii) the TSP and iv) the NSP at 30 and 45 °C. c) G' of SMPs at various temperatures for different SA-to-LMA monomer weight ratios. d) 3D laser confocal microscopy images of i) porcine skin and ii) the adapted TSP. e) 2D cross-sectional profiles of i) porcine skin, ii) SMPs with SNPs after skin adaptation and recovery, and iii) SMPs without SNPs after skin adaptation and recovery. R_q represents the root mean square (RMS) roughness.

to a higher T_m (Figures 2c and S10, Supporting Information). For example, the SMP with a 9:1 SA ratio had a T_m of 48.2 °C, posing potential thermal damage to the epidermis, while the SMP with a 3:7 ratio had a T_m of 21.1 °C, remaining in a rubbery state at room temperature. 3D laser confocal microscopy confirmed the TSP's ability to conform to rough porcine skin at elevated temperatures and retain this adapted state upon cooling (Figure 2d).

Beyond surface adaptability, the TSP is designed for complete shape recovery when heated above T_m, enabling easy self-detachment from the skin and reuse of the patch. To ensure rapid self-detachment, sufficient recovery strength is required to overcome the adhesive forces between the TSP and skin, which is related to the patch's modulus in its rubbery state.[15b,25] SNPs were incorporated into the SMP to enhance its G' in the rubbery state. The pristine rigid SMP segment had a G' of 30.3 kPa and recovery strength of 25.5 kPa. With 6 wt.% SNPs added to the rigid SMP, the G' increased to 118.9 kPa and recovery strength to 105.8 kPa (Figures S4, S11, S12 and Movie S1, Supporting Information). This improvement is attributed to interactions between the silanol and hydroxyl groups of the SNPs and the acrylate groups in the SMP.[26] The SNPs-reinforced SMP demonstrated full shape recovery after exposure to 45 °C following skin attachment (Figure 2e-i,ii and Movie S2, Supporting Information), while the pristine SMP struggled to recover its shape, even upon heating (Figure 2e-iii).

2.3. Switchable Adhesion

To evaluate the on-demand adhesion switchability of the TSP, we measured its pull-off adhesion performance on porcine skin at two temperatures (30 and 45 °C), varying the SNP content

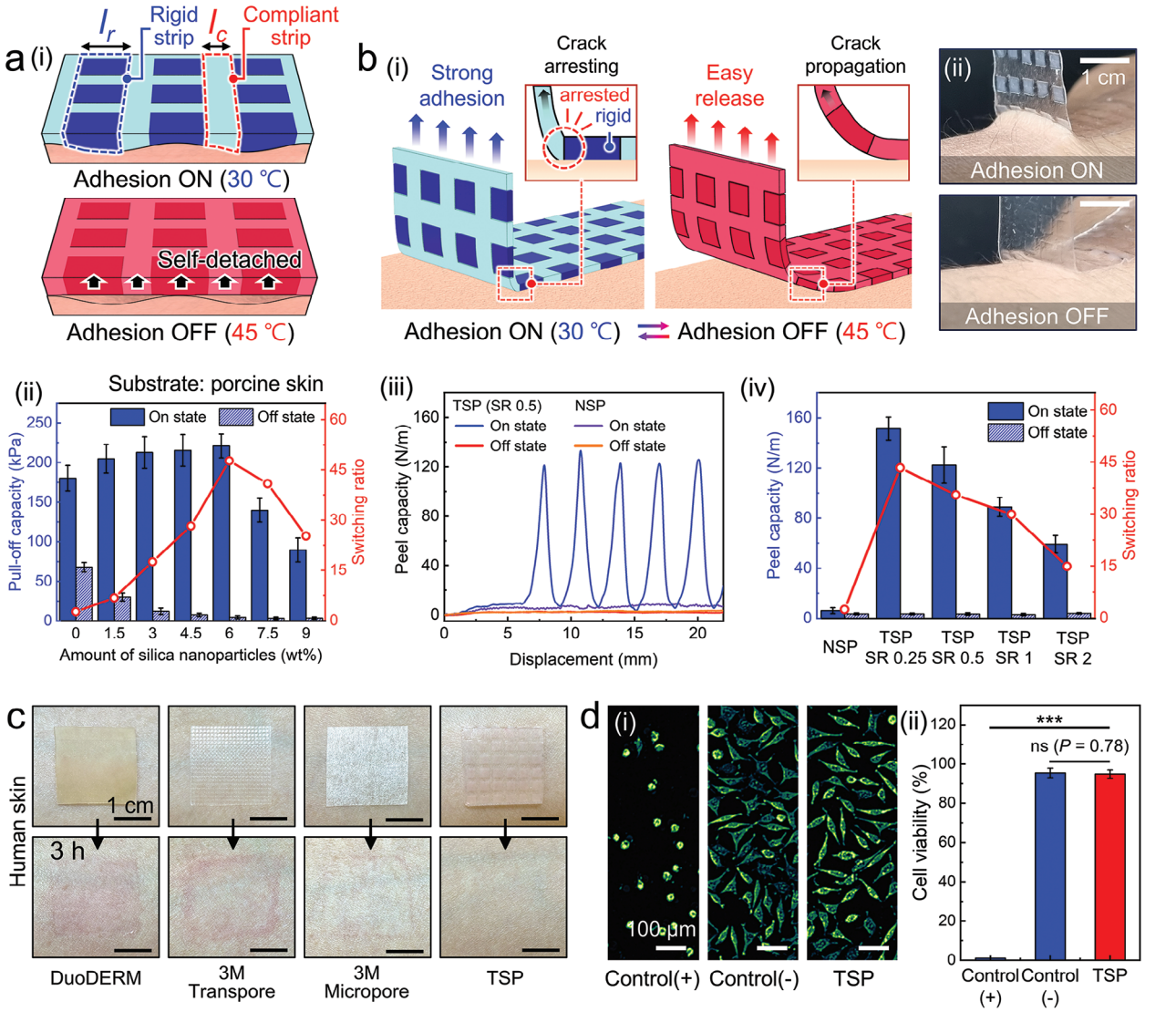

Figure 3. Adhesion performance of the TSP. a) i) Schematic illustrating the pull-off adhesion switching mechanism of the TSP. ii) Pull-off adhesion and adhesion switching ratios of the TSP on porcine skin as a function of SNP content in the "on" (30 °C) and "off" (45 °C) states. Retraction speed: 2 mm s^{-1}. b) i) Schematic showing the peel adhesion switching and crack arresting mechanisms of the TSP. ii) Photographs showing strong skin adhesion in the "on" state (top) and easy release in the "off" state (bottom). iii) Peel adhesion strengths of the TSP and NSP in "on" and "off" states during peeling. Retraction speed: 1 mm s^{-1}. iv) Peel adhesion strengths and adhesion switching ratios of the TSP as a function of *SR* in both states. c) Comparisons of skin irritation after 3 h of attachment using TSP and other skin adhesives. d) In vitro cytotoxicity tests of the TSP using murine fibroblasts after 48 h of culture: i) microscopy images and ii) quantitative analysis of cell viability. Statistical significance and *P* values were evaluated by unpaired Student's *t*-test ($n = 3$; ns, not significant; $^{***}P < 0.001$).

(**Figures** 3a-i and S13, Supporting Information). As the SNP content increased from 0 wt.% to 6 wt.%, pull-off adhesion in the "on" state (30 °C) slightly improved due to the higher *G'* at 30 °C (Figures 3a-ii and S4, Supporting Information). However, when SNP content exceeded 7.5 wt.%, pull-off adhesion dropped sharply due to the relatively high *G'* (172.9 kPa) at 45 °C, which impedes conformal adaptation to rough skin topography under the preload conditions (preload: 20 kPa). Pull-off adhesion in the "off" state (45 °C) consistently decreased with increasing SNP content, attributed to the enhanced recovery strength of SMPs with higher SNP concentrations. The TSP with 6 wt.% SNP exhibited the highest pull-off switching ratio of 47.7, with an "on" state of 221 kPa and an "off" state of 4.6 kPa on skin (Figure 3a-ii). The TSP maintains its adhesion performance and switchability for over 500 cycles of attachment and detachment (Figure S14, Supporting Information), while commercial skin adhesives lose adhesion after a single use and lack any adhesion switching capability. Additionally, the TSP demonstrated excellent pull-off adhesion of 200.8 kPa even on wet skin (Figure S15, Movies S3 and S4, Supporting Information).

Next, we examined the peel adhesion capacity of the TSP (Figure 3b-i,ii). For conventional skin adhesives made of homogeneous materials, once a crack initiates at the bonded interfaces, it tends to propagate continuously, often resulting in low peel

adhesion.[27] In contrast, the TSP's heterogeneous structure offers superior crack-arresting capabilities. When the crack front moves from a compliant strip to a rigid strip, it is effectively arrested (Figures 3b-i and S16, Supporting Information). This occurs because, as the peel front reaches the rigid strip, a large portion of the peel force is converted into bending strain energy in the stiffer region, reducing the driving force for crack propagation.[28] In the "on" state, the TSP showed a significantly higher peel adhesion of 122.3 N m^{-1} at the rigid strip, compared to just 5.8 N m^{-1} at the compliant strip (Figure 3b-iii). The rigid and compliant segments measured 2 and 1 mm, respectively, establishing the spacing ratio ($SR = l_c/l_r$) used in this study. Notably, when the TSP switched to the "off" state, peel adhesion dropped sharply to 3.4 N m^{-1} (Figure 3b-iii), just 4% of the "on" state value. Photographs in Figure 3b-ii (Figure S17, Supporting Information) highlight the strong skin adhesion of the TSP in the "on" state and minimal adhesion in the "off" state.

We also investigated the peel adhesion of TSP with different *SR*s (0.25, 0.5, 1, and 2) (Figure 3b-iv). The rigid segment length (l_r) was fixed at 2 mm, based on the characteristic length of the rigid strip ($l_{ch,r} = 1.1$ mm) (see Figure S18 and Note S1, Supporting Information for details). Experimental results showed that TSPs with smaller *SR*s exhibited higher peel adhesion in the "on" state, due to the larger proportion of rigid segments contributing to increased adhesion strengths. However, in the extreme case of an NSP with no compliant segment, peel adhesion significantly decreased to 6.1 N m^{-1} (Figure 3b-iv). This occurred because the NSP, lacking a compliant segment, could not deform sufficiently to dissipate peel energy effectively, leading to rapid detachment from the substrate under peeling. The peel adhesion can be controlled by modulating both design (spacing ratio) and temperature, demonstrating the adhesion programmability (Figure S19, Supporting Information).

It is important to note that the proposed TSP demonstrates exceptional skin adhesion in both pull-off and peel tests, significantly outperforming commercial skin adhesives (Figure S20, Supporting Information). The TSP exhibited strong pull-off adhesion, ranging from 442.8 to 1070.2 kPa, and peel adhesion between 167.9 to 200.9 N m^{-1} on engineered substrates (Figure S21, Supporting Information). Additionally, the TSP exhibited stronger adhesion on rougher surfaces due to its phase-change-based adhesion mechanism (Figure S22, Supporting Information). Furthermore, the TSP showed excellent skin compatibility, with no irritation or damage after up to 48 h of attachment, in contrast to commercial skin adhesives, which caused visible irritation (Figures 3c and S23, Supporting Information). The TSP's high biocompatibility was further confirmed by cell viability tests (Figures 3d and S24, Supporting Information), underscoring its potential for safe, long-term skin contact applications.

2.4. Dynamic Motion Adaptability and Deformability

We explored the deformability and motion adaptability of the TSP under dynamic conditions (**Figure 4**). As shown in Figure 4a, the TSP exhibited significant deformability at room temperature, with strains (ϵ) exceeding 100%, reaching a maximum of 219.6% (Figures 4a-i,b and S25, Supporting Information). It could also twist (θ_{twist}) by over 540°, achieving a maximum twisting angle ($\theta_{twist,max}$) of 3420° for a TSP with an *SR* of 2.0 (Figures 4a-ii and S26, Supporting Information). This remarkable deformability is due to the TSP's tessellated architecture. When attached to an inflating balloon, deformation occurred primarily at the compliant joints, allowing an areal strain (ϵ_a) exceeding 150%, with a maximum areal strain ($\epsilon_{a,max}$) of 550.4% for a TSP with an SR of 2.0, all while maintaining strong adhesion to the balloon surface (Figures 4a-iii and S26, Supporting Information). In contrast, the NSP could neither stretch nor twist effectively at room temperature (Figures S25 and S27, Supporting Information) and delaminated from the balloon surface during inflation due to a mismatch in allowable strains (Figure S28, Supporting Information).

Figure 4b shows the stress-strain curves for TSPs with varying *SR*s, as well as the NSP, measured at room temperature. As *SR* increased, the TSP showed greater stretchability and a lower elastic modulus due to the larger proportion of compliant regions. In contrast, the NSP had a much higher elastic modulus and a significantly lower elongation at break (ϵ_b) of 14.4% (Figure S29, Supporting Information). The ϵ_b of the TSP with a *SR* of 2.0 was 219.6%, a 15.3-fold increase compared to the NSP (14.4%). The effective elastic modulus (E_{eff}) of the TSP can be theoretically calculated as (see Note S1, Supporting Information for more details)

$$E_{eff} = \left(\frac{1}{E_r + (SR)\,E_c} + \frac{SR}{E_c + (SR)\,E_c} \right)^{-1} \quad (1)$$

where E_r and E_c are the elastic moduli of the rigid and compliant segments, respectively, and *SR* is the spacing ratio. The calculated E_{eff} of the TSP with *SR*s of 0.25, 0.5, 1.0, and 2.0 were 763.6, 462, 309.4, and 232.5 kPa, respectively, which aligned well with the experimental results (inset of Figure 4b). This value is comparable to that of human skin (E_{skin} = 420 kPa) (Figure S29, Supporting Information).[29] In contrast, the E_{eff} of the NSP is much higher (35.9 MPa).

We conducted finite element analysis (FEA) to compare the adaptability of the TSP and NSP on dynamic surfaces (Figure 4c). During the simulation, both TSP and NSP samples were attached to a substrate that was gradually stretched. The NSP showed significant stress concentration at the contact interface with the substrate (Figure 4c), indicating a high risk of delamination. In contrast, the TSP's tessellated structure allowed a more uniform stress distribution across the interface, preventing delamination even as the substrate deformed. Tensile tests supported these simulation results (Figure 4d). Both NSP and TSP were adhered to artificial skin made of PDMS, designed to mimic the surface roughness of porcine skin. Initially, both patches adhered well with no substrate stretching ($\epsilon = 0\%$). However, the NSP began to delaminate at the edges with just 5% strain (Figures 4d-i and S30, Supporting Information), and complete delamination occurred at 60% strain. In contrast, the TSP maintained strong adhesion even at 60% strain (Figures 4d-ii and S30, Supporting Information).

Finally, we assessed the dynamic motion adaptability of both TSP and NSP on human skin. Both initially adhered well to the dorsal wrist. However, during wrist movement, the NSP quickly delaminated (Figure 4e-i), while the TSP maintained close skin contact, demonstrating excellent deformability and motion adaptability (Figures 4e-ii and S31 and Movie S3, Supporting Information). When applied to the dorsal finger joints,

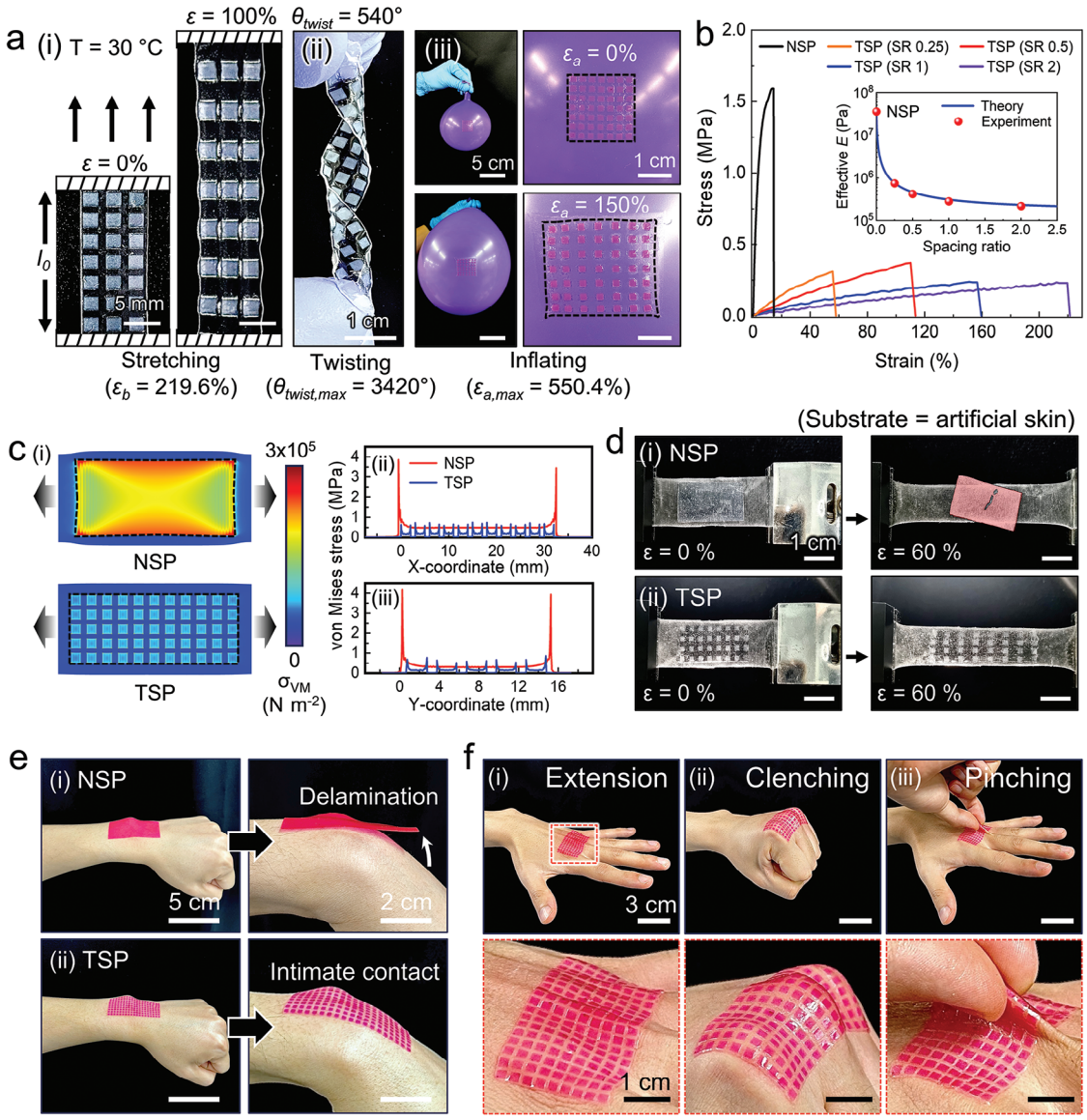

Figure 4. Mechanical properties and motion adaptability of the TSP. a) Photographs showing the TSPs under various mechanical deformations: i) stretching, ii) twisting, and iii) inflating. b) Stress–strain curves for TSPs with different SRs. The inset shows a comparison between the theoretically and experimentally obtained effective elastic modulus of the TSPs with various SRs. c) FEA simulation demonstrating the motion adaptability differences between the NSP and TSP: i) Stress distribution at the interface between the patch and the stretchable substrate under longitudinal tensile strain of 25%, ii) Quantitative Von Mises stress distribution across the interface in the x-direction, and iii) y-direction. d) Photographs showing the motion adaptability of the i) NSP and ii) TSP attached to artificial skin when subjected to tensile strains. e) Photographs showing i) the limited motion adaptability of the NSP and ii) the outstanding motion adaptability of the TSP during wrist bending motion. f) Photographs depicting the remarkable motion adaptability of the TSP attached to dorsal finger joints under various deformation conditions: i) extension, ii) clenching, and iii) pinching. All experiments were conducted at 30 °C.

which experience significant strain,[30] the TSP adhered firmly and adapted well to dynamic hand movement such as extension, clenching and pinching (Figure 4f).

2.5. Health Monitoring Application

To integrate the TSP into wearable electronic application, conductive AgNWs (diameter: 20 nm, length: 20 µm) were uniformly deposited on the TSP surface to form flexible electrodes, using automated large-area spray coating and transfer printing techniques (**Figures** 5a and S32, Supporting Information). These electrodes feature circular islands on rigid segments, connected by serpentine lines to enhance mechanical stretchability (Figure 5a-i,ii). Partially embedded within the SMP layer of the TSP (Figure S33, Supporting Information), the electrodes enable direct electrical contact with the skin. Despite the presence of AgNWs, the TSP electrode maintained excellent surface adaptability and adhesion to the skin (Figures 5a-iii,iv and S34, Supporting Information). Additionally, the TSP electrode with AgNW coating

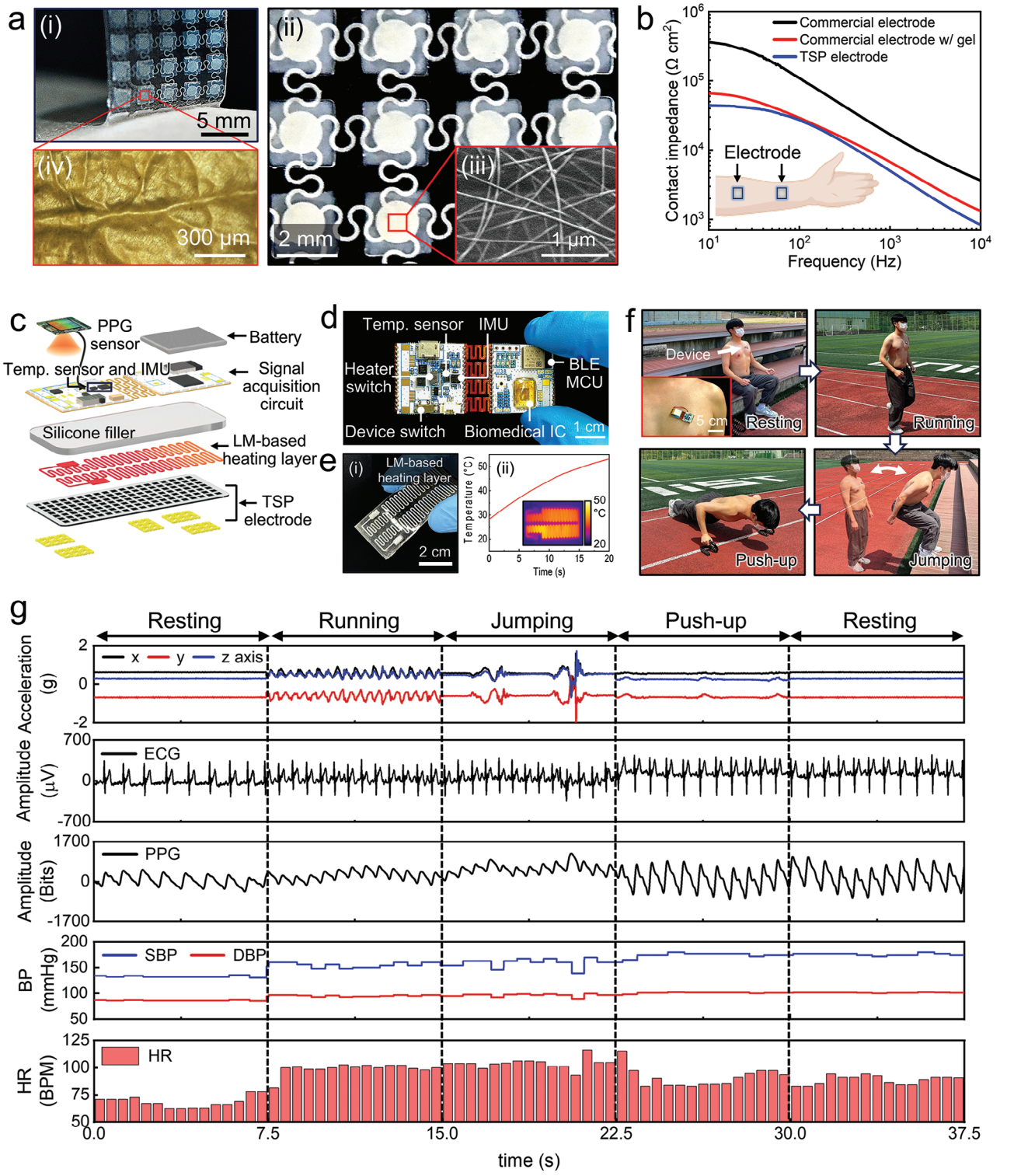

Figure 5. Application of the TSP in integrated skin-interfaced electronics for wireless health monitoring. a) i) Photograph of the fabricated TSP electrode with embedded AgNWs attached to skin, ii) Enlarged view of the TSP electrode, iii) SEM image of the AgNW network, and iv) Optical microscopy image of the electrode surface morphology after adaptation to skin. b) Comparison of contact impedance between the TSP electrode and a commercial Ag/AgCl electrode. c) Schematic illustrating the TSP integrated skin-mountable electronics with a multi-layered design incorporating various functional elements. d) Photograph of the wireless data acquisition circuit. e) i) Photograph of the LM-based flexible heating layer, ii) Temperature profile of the LM-based heater over time (bias voltage = 4 V). The inset shows IR thermography of the heater after applying 4 V for 10 s. f) Photographs of a human volunteer wearing the TSP-integrated skin-mountable electronic device on the chest skin during various physical activities. g) Various physiological signals measured during different activities. From top to bottom: acceleration, ECG, PPG, blood pressure (SBP and DBP), and heart rate (HR).

demonstrated a low sheet resistance (R_s) and contact resistance (R_c) performance (see Figures S34–S37 and Note S1, Supporting Information for details).

The TSP electrode also exhibited superior skin-electrode contact impedance compared to commercial electrodes (Figure 5b; Figure S38, Supporting Information). Across a frequency range of 10^1 to10^4 Hz, the TSP electrode showed lower impedance than commercial Ag/AgCl electrodes, even with additional conductive gels. Notably, the TSP electrode maintained stable contact impedance over 7 days (Figure S38, Supporting Information), whereas Ag/AgCl electrodes experienced a significant impedance increase by the second day due to hydrogel drying. Furthermore, the TSP electrode maintained high SNRs above 20 dB, even during dynamic body motion (see Figure S39 and Note S1, Supporting Information for details).

The TSP electrode excels in key properties, including switchable skin adhesion, stretchability and adaptability, electrical conductivity, SNRs, and skin compatibility, making it ideal for advanced skin-interfaced electronic applications. To demonstrate its potential, we developed a skin-mountable, wireless cardiovascular health monitoring device. This device features a multi-layered design incorporating the TSP electrode, a flexible liquid metal (LM) heater, silicone filler, wireless signal acquisition circuits, photoplethysmography (PPG) and temperature sensors, an inertial measurement unit (IMU), and a battery (Figures 5c and S40, Supporting Information). The TSP electrode collects biopotential and impedance signals, which are transmitted to the wireless signal acquisition circuit. A temperature sensor prevents overheating of the heater, while the IMU monitors accelerations from body motion. The LM heater controls the phase transition and adhesion switching of the TSP layer via resistive heating, reaching 45 °C within 10.6 s at 4 V (Figures 5e and S41, Supporting Information). The silicone filler mitigates strain mismatch between the TSP and rigid components. Figure 5d shows the wireless signal acquisition circuit, measuring 24 mm x 60 mm (see Figure S42 and Note S1, Supporting Information for details). The circuit is divided into two sections connected by a flexible hinge to improve flexibility.

This integrated device was applied to a human subject's chest to continuously monitor cardiovascular health by recording 3-axis acceleration, ECG, PPG, blood pressure (BP), and heart rate (HR) during various activities (Figure 5f). Despite its bulky size and weight, the device remained firmly attached to the skin. Using this TSP-integrated device, systolic BP (sBP) and diastolic BP (dBP) were estimated in real-time based on pulse arrival time (PAT), which is the time difference between the R-wave of the ECG and the systolic peak of the PPG signals. HR was similarly calculated in real-time using the intervals between the R-waves on the ECG. During various activities, including resting, running, jumping, and push-ups, the device precisely and continuously monitored 3-axis acceleration, ECG, PPG, BP, and HR (Figure 5g). The multiple biosignals acquired remained consistently stable regardless of the activity or motion, thanks to the TSP's excellent mechanical, adhesive, and electrical properties. Moreover, the TSP-integrated device demonstrated reusability on different body locations (Figure S43, Supporting Information). When sequentially attached to areas such as the chest, forearm, and forehead, it maintained stable adhesion and accurately measured various ExG signals.

3. Conclusions

In summary, we have introduced a deterministic skin adhesive patch that strategically integrates heterogeneous phase change elements in a tessellated configuration. This approach simultaneously achieves unparalleled adhesive, mechanical, and electrical functionalities, addressing several critical limitations of existing skin-interfaced electronics. Specifically, the multifunctional TSP demonstrated impressive pull-off (1070.2 kPa) and peel adhesion (200.9 N m^{-1}), remarkable adhesion switchability (47.7), high reusability (>500 cycles), and a low effective modulus (218.8 kPa) that closely matches the modulus (140–600 kPa) of human skin.[31] Furthermore, the TSP exhibited high mechanical deformability (ϵ_b = 219.6%, $\theta_{twist,max}$ = 3420°, and $\epsilon_{a,max}$ = 550.4%), low R_c (38.8 kΩ μm), low skin contact impedance (44.1 kΩ at 10 Hz), and high SNRs (22.5 B for ECG signals). These capabilities surpass those of many existing skin adhesives and commercial electrodes (Table S1, Supporting Information).

The synergistic combination of exceptional adhesive performance and mechanical deformability enabled the TSP to achieve remarkable motion adaptiveness during dynamic movements while maintaining stable skin attachment. The adhesion switching capacity allowed for the repeated use of the patch and easy, on-demand release from the skin via resistive heating. The mechanical robustness and flexibility of the TSP facilitated easy handling and application of the device. Importantly, the TSP demonstrated excellent skin compatibility, making it suitable for prolonged skin contact applications.

Leveraging its remarkable skin adhesion, high mechanical deformability and durability, outstanding electrical properties, and skin compatibility, the TSP enabled the seamless integration of various key electronic components. The resulting TSP-based, integrated skin-mountable device could be securely, reversibly, and repeatedly mounted on the skin, accommodating highly dynamic body motions. It precisely and wirelessly detected various biometric signals, including acceleration, ECG, EMG, EOG, EEG, BP, and HR with exceptional SNRs (22.5 dB for ECG signals). We anticipate that the multifunctional skin adhesive patch, with its unique design and compatibility with various electronics, will significantly contribute to the development of highly functional, comfortable, and user-friendly wearable technologies.

4. Experimental Section

Fabrication of the Tessellated Skin Patch: First, the SMP nanocomposite was prepared by mixing SA and LMA in a heated water bath at 60 °C. The weight ratio of SA to LMA was adjusted to control the thermomechanical properties. 70 mg of EGDMA and 80 mg of 2,2-dimethoxy-2-phenylacetophenone were added to 10 g of the SA/LMA mixture and sonicated for 20 min to eliminate any residuals. Different amounts of SNPs (0, 1.5, 3, 4.5, 6, 7.5, and 9 wt.%) were then blended into the mixture. To prepare the TSP, a screen-printing technique was employed (Figure S7, Supporting Information). The patterned shadow mask was fixed to a silanized glass substrate. The prepared SMP nanocomposite solution for the rigid segment, with a 7:3 weight ratio of SA to LMA, was then applied to the shadow mask and spread with a blade to ensure it covered the entire area (step 1 in Figure S7, Supporting Information). The substrate was cooled to 10 °C to temporarily maintain the square segment shapes, then the shadow mask was removed. Subsequently, the SMP nanocomposite solution for the compliant segment, with a 3:7 ratio of SA to LMA, was applied to fill the spaces between the rigid segments array. To form a

conductive and flexible electrode onto the TSP, an AgNW solution was selectively sprayed onto a PET substrate using a shadow mask with the desired circuit patterns (step 2 in Figure S7, Supporting Information). The deposition dose of AgNWs was controlled by adjusting the concentration of the solution. Finally, the pre-cured TSP from step 1 was integrated with the PET film containing the AgNWs electrode. The assembly was cured under UV irradiation (λ = 365 nm, dose = 300 mJ cm^{-2}) for 1 h, yielding the AgNWs-integrated TSP electrode (step 3 in Figure S7, Supporting Information).

Mechanical Tests: The dynamic mechanical analysis (DMA) test was conducted using a DMA tester (Q800, TA Instrument, USA) in tension mode under a temperature sweep. The rectangular sample (15 mm x 7 mm x 1 mm) was tested under an oscillatory strain of 0.2% at a frequency of 1 Hz. The temperature was swept from 15 to 70 °C at a rate of 1 °C min^{-1}. To quantify the shape memory effect, a cyclic thermomechanical test was conducted using the DMA tester. The sample was initially heated to 45 °C and then stretched under an external force. After cooling to 30 °C, the temporary shape was fixed, and the force was released. During the recovery process, the stress-free condition was applied to estimate the shape recovery ratio, while the constant-strain condition was used to determine the recovery strength. Additionally, the uniaxial tensile test was performed with the mechanical tester (UniVert, CellScale, Canada) to determine the elastic modulus and elongation at break. The sample (25 mm x 12 mm x 0.2 mm) was stretched at a stretching rate of 5 mm min^{-1}.

Adhesion Tests: The pull-off and peel adhesion tests were conducted using a mechanical tester (Univert, Cellscale, Canada). For the pull-off adhesion test, a custom-built setup was utilized, consisting of a substrate holder, an adhesive sample holder, and a vertically movable jig (Figure S13, Supporting Information). Target substrates were affixed to the substrate holder using double-sided tape (3M, USA), while adhesive samples were secured to the adhesive sample holder, facing downwards, also using double-sided tape. The adhesive samples were then brought into contact with the substrates under a preload of 20 kPa applied via weights. Subsequently, the adhesive sample holder was connected to the vertically movable jig via a fishing line. Adhesive forces were measured as the jig was retracted upward at a rate of 2 mm s^{-1} until the samples detached from the substrates. For the peel adhesion test, the 90-degree peel test was conducted at a retraction rate of 1 mm s^{-1} (Figure S13, Supporting Information). Target substrates were secured to a horizontally slidable substrate holder using double-sided tape. The adhesive samples were brought into contact with the substrates under a preload of 20 kPa applied via weights. The end of the adhesive samples was fixed to a vertically movable jig. As the jig moved upward, the adhesive forces were measured. For both pull-off and peel adhesion tests of TSP and NSP, the "on" state adhesion was evaluated by bringing the adhesives into contact with the substrates under a preload of 20 kPa for 5 s at a rubbery state of 45 °C, heated with a heat gun (GHG 20–63, BOSCH, Germany), then cooling to 30 °C while maintaining the preload to ensure shape fixation. In the "off" state, the adhesion was measured after reheating to 45 °C without applying preload.

Electrical Characterizations: The sheet resistance (R_s) of the TSP electrode was assessed using a four-point probe surface resistivity meter (CMT-SR1000N, Advanced Instrument Technology, Republic of Korea). For contact resistance (R_c) measurement, a four-point probe pattern was created by sputtering gold onto polyurethane acrylate (PUA) substrates. These PUA substrates, with various roughness levels, were fabricated through a replica molding process using sandpapers (R_q = 66, 18.3, and 10.3 µm). R_c values were measured by attaching the TSP electrodes to the prepared four-point probe-patterned PUA substrates after applying different external pressures (no pressure, 2 and 50 kPa), with and without surface adaptation. The variations in R_c of the TSP samples in contact with the four-point probe-patterned PUA substrates were also evaluated under bending conditions with different radii of curvature (5–20 mm). For skin contact impedance measurement, two electrodes were placed on the forearm, positioned 5 cm apart. The electrode types included Ag/AgCl electrodes (2223H, 3 M, USA) with and without additional conductive gel (Signa Gel, Parker Labs, USA), as well as TSP electrodes. These electrodes were directly connected to the LCR meter (E4980A, Keysight, USA) to measure and record the skin contact impedance data. Measurements were taken across a frequency range of 10^1 to 10^4 Hz.

Fabrication of Skin-Mountable Health Monitoring Device: To prepare the wireless signal acquisition circuit, electronic design automation software (OrCAD version 17.4, Cadence Design Systems, USA) was used to create the circuit schematic and design the PCB. A custom-designed IC was integrated into the PCB using chip-on-board technology, while the other active and passive components were assembled using surface-mount technology. These components included a BLE MCU (STM32WB5MMG, STMicroelectronics, Switzerland), a PPG sensor (SFH 7072, ams OSRAM, Austria), a temperature sensor (TMP 117, TI, USA), an IMU (LIS3DSH, STMicroelectronics, Switzerland), and a buck-boost converter (TPS63000, TI, USA). The flexible LM heater was prepared by a 3D printing process (BIOX bioprinter, CELLINK, Sweden) using eutectic gallium-indium (EGaIn) on a thin low modulus PDMS layer (30:1 base resin-to-curing agent ratio, thickness: 30 µm). The printed EGaIn was then encapsulated with a low modulus PDMS, which also acts as a silicone filler (Figure 5c, thickness: 2 mm). The prepared signal acquisition circuit and the TSP electrode were electrically connected to each other by self-adhering the connection lines of the TSP electrode to the flat electrodes located on the backside of the signal acquisition circuit (Figure S40, Supporting Information), resulting in highly strong and stable interface (Figure S44, Supporting Information). The LM heater covered with the silicone filler was inserted between the circuit and the TSP electrode (Figure 5c).

Statistical Analysis: Datasets were analyzed using unpaired Student's *t*-test for comparisons between two conditions, and one-way ANOVA followed by Tukey's multiple comparison test was performed to compare three or more conditions. In all cases, *P* values less than 0.05 were considered statistically significant. Calculations were carried out using SPSS version 29.0.2.0. The means ± standard deviation for each dataset was calculated from at least three experiments.

Institutional Review Board (IRB) Approval for the Study on Human Subjects: All experiments involving human research participants were conducted in accordance with the protocol approved by the IRB of Ulsan National Institute of Science and Technology (UNISTIRB-23-061-A). Informed written consent had been obtained from all participants.

Supporting Information

Supporting Information is available from the Wiley Online Library or from the author.

Acknowledgements

G. C. and J. K. contributed equally to this work. This work was supported by National Research Foundation (NRF) of Korea grant funded by the Korea government (MSIT) (NRF-2021R1A2C3006297 and RS-2024-00432685) and the Technology Innovation Program (00144157) funded by the Ministry of Trade, Industry & Energy (MOTIE) of Korea. This work was also supported by the National Institute of Ecology (NIE-B-2024-18).

Conflict of Interest

The authors declare no conflict of interest.

Data Availability Statement

The data that support the findings of this study are available from the corresponding author upon reasonable request.

Keywords

shape memory polymer, skin adhesive, skin-interfaced, stiffness variable polymer, wearable device

Received: August 19, 2024
Revised: October 8, 2024
Published online:

[1] K. Nan, V. R. Feig, B. Ying, J. G. Howarth, Z. Kang, Y. Yang, G. Traverso, *Nat. Rev. Mater.* **2022**, *7*, 908.
[2] a) S. Wang, J. Xu, W. Wang, G.-J. N. Wang, R. Rastak, F. Molina-Lopez, J. W. Chung, S. Niu, V. R. Feig, J. Lopez, T. Lei, S.-K. Kwon, Y. Kim, A. M. Foudeh, A. Ehrlich, A. Gasperini, Y. Yun, B. Murmann, J. B.-H. Tok, Z. Bao, *Nature* **2018**, *555*, 83; b) R. Herbert, H.-R. Lim, S. Park, J.-H. Kim, W.-H. Yeo, *Adv. Healthcare Mater.* **2021**, *10*, 2100158.
[3] H. Lee, T. K. Choi, Y. B. Lee, H. R. Cho, R. Ghaffari, L. Wang, H. J. Choi, T. D. Chung, N. Lu, T. Hyeon, S. H. Choi, D.-H. Kim, *Nat. Nanotechnol.* **2016**, *11*, 566.
[4] a) Y. Yu, J. Li, S. A. Solomon, J. Min, J. Tu, W. Guo, C. Xu, Y. Song, W. Gao, *Sci. Robot.* **2022**, *7*, eabn0495; b) S. Ding, D. Zhao, Y. Chen, Z. Dai, Q. Zhao, Y. Gao, J. Zhong, J. Luo, B. Zhou, *Adv. Sci.* **2024**, *11*, 2302782; c) S. Park, D. K. Kang, D. Lee, G. Choi, J. Kim, C. Lee, M. Seong, M. D. Bartlett, H. E. Jeong, *Sci. Adv.* **2024**, *10*, eadq3438.
[5] a) C. Wang, H. Wang, B. Wang, H. Miyata, Y. Wang, M. O. G. Nayeem, J. J. Kim, S. Lee, T. Yokota, H. Onodera, T. Someya, *Sci. Adv.* **2022**, *8*, eabo1396; b) S.-H. Sunwoo, K.-H. Ha, S. Lee, N. Lu, D.-H. Kim, *Annu. Rev. Chem. Biomol. Engineer.* **2021**, *12*, 359.
[6] F. Ershad, A. Thukral, J. Yue, P. Comeaux, Y. Lu, H. Shim, K. Sim, N.-I. Kim, Z. Rao, R. Guevara, L. Contreras, F. Pan, Y. Zhang, Y.-S. Guan, P. Yang, X. Wang, P. Wang, X. Wu, C. Yu, *Nat. Commun.* **2020**, *11*, 3823.
[7] a) T. R. Ray, J. Choi, A. J. Bandodkar, S. Krishnan, P. Gutruf, L. Tian, R. Ghaffari, J. A. Rogers, *Chem. Rev.* **2019**, *119*, 5461; b) P. Won, J. J. Park, T. Lee, I. Ha, S. Han, M. Choi, J. Lee, S. Hong, K.-J. Cho, S. H. Ko, *Nano Lett.* **2019**, *19*, 6087.
[8] a) Y. Morikawa, S. Yamagiwa, H. Sawahata, R. Numano, K. Koida, T. Kawano, *Adv. Healthcare Mater.* **2019**, *8*, 1900939; b) T. Someya, M. Amagai, *Nat. Biotechnol.* **2019**, *37*, 382; c) S. Park, G. Choi, M. Kang, W. Kim, J. Kim, H. E. Jeong, *Microsyst. Nanoeng.* **2023**, *9*, 153; d) S. Ji, C. Wan, T. Wang, Q. Li, G. Chen, J. Wang, Z. Liu, H. Yang, X. Liu, X. Chen, *Adv. Mater.* **2020**, *32*, 2001496; e) S. H. Choi, B. J. Lee, S. Y. Lee, *Skin Res. Technol.* **2023**, *29*, e13288; f) R. Zhao, S. Lin, H. Yuk, X. Zhao, *Soft Matter* **2018**, *14*, 2515.
[9] a) K. R. Jinkins, S. Li, H. Arafa, H. Jeong, Y. J. Lee, C. Wu, E. Campisi, X. Ni, D. Cho, Y. Huang, J. A. Rogers, *Sci. Adv.* **2022**, *8*, eabo0537; b) I. Hwang, H. N. Kim, M. Seong, S.-H. Lee, M. Kang, H. Yi, W. G. Bae, M. K. Kwak, H. E. Jeong, *Adv. Healthcare Mater.* **2018**, *7*, 1800275.
[10] a) A. Kochanke, K. Krämer, C. Üffing, A. Hartwig, *Int. J. Adhes. Adhes.* **2021**, *111*, 102980; b) S. J. Wu, H. Yuk, J. Wu, C. S. Nabzdyk, X. Zhao, *Adv. Mater.* **2021**, *33*, 2007667.
[11] Y. Kim, J. M. Suh, J. Shin, Y. Liu, H. Yeon, K. Qiao, H. S. Kum, C. Kim, H. E. Lee, C. Choi, H. Kim, D. Lee, J. Lee, J.-H. Kang, B.-I. Park, S. Kang, J. Kim, S. Kim, J. A. Perozek, K. Wang, Y. Park, K. Kishen, L. Kong, T. Palacios, J. Park, M.-C. Park, H.-J. Kim, Y. S. Lee, K. Lee, S.-H. Bae, et al., *Science* **2022**, *377*, 859.
[12] Z. Jiang, N. Chen, Z. Yi, J. Zhong, F. Zhang, S. Ji, R. Liao, Y. Wang, H. Li, Z. Liu, Y. Wang, T. Yokota, X. Liu, K. Fukuda, X. Chen, T. Someya, *Nat. Electron.* **2022**, *5*, 784.
[13] J. Kim, S. Yoo, C. Liu, S. S. Kwak, J. R. Walter, S. Xu, J. A. Rogers, *Nat. Rev. Bioeng.* **2023**, *1*, 631.
[14] a) H. Cheng, S. Wang, *J. Appl. Mech.* **2014**, *81*, 044501; b) Y. Zhang, T. H. Tao, *Adv. Mater.* **2019**, *31*, 1905767.
[15] a) H. Cho, G. Wu, J. C. Jolly, N. Fortoul, Z. He, Y. Gao, A. Jagota, S. Yang, *Proc. Natl. Acad. Sci. USA* **2019**, *116*, 13774; b) C. Linghu, Y. Liu, Y. Y. Tan, J. H. M. Sing, Y. Tang, A. Zhou, X. Wang, D. Li, H. Gao, K. J. Hsia, *Proc. Natl. Acad. Sci. USA* **2023**, *120*, e2221049120.
[16] M. D. Bartlett, S. W. Case, A. J. Kinloch, D. A. Dillard, *Prog. Mater. Sci.* **2023**, *137*, 101086.
[17] C. Son, S. Kim, *ACS Appl. Mater. Interfaces* **2021**, *13*, 56718.
[18] a) L. Khandeparker, A. C. Anil, *Int. J. Adhes. Adhes.* **2007**, *27*, 165; b) C. Y. Hui, R. Long, K. J. Wahl, R. K. Everett, *J. R. Soc. Interface* **2011**, *8*, 868; c) Z. Xu, Z. Liu, C. Zhang, D. Xu, *J. Appl. Polym. Sci.* **2022**, *139*, e52894.
[19] a) I. H. Chen, J. H. Kiang, V. Correa, M. I. Lopez, P. Y. Chen, J. McKittrick, M. A. Meyers, *J. Mech. Behav. Biomed. Mater.* **2011**, *4*, 713; b) P. Fratzl, O. Kolednik, F. D. Fischer, M. N. Dean, *Chem. Soc. Rev.* **2016**, *45*, 252.
[20] a) M. Gao, H. Wu, R. Plamthottam, Z. Xie, Y. Liu, J. Hu, S. Wu, L. Wu, X. He, Q. Pei, *Matter* **2021**, *4*, 1962; b) H. J. Park, M. Kim, J. Lee, M. K. Kwak, *Adv. Sci.* **2024**, *11*, 2309393; c) Z. Zhao, S. Zhuo, R. Fang, L. Zhang, X. Zhou, Y. Xu, J. Zhang, Z. Dong, L. Jiang, M. Liu, *Adv. Mater.* **2018**, *30*, 1804435; d) M. Seong, K. Sun, S. Kim, H. Kwon, S.-W. Lee, S. C. Veerla, D. K. Kang, J. Kim, S. Kondaveeti, S. M. Tawfik, H. W. Park, H. E. Jeong, *Nat. Commun.* **2024**, *15*, 7929.
[21] a) M. A. Haq, Y. Su, D. Wang, *Mater. Sci. Eng. C* **2017**, *70*, 842; b) H. Yuk, T. Zhang, G. A. Parada, X. Liu, X. Zhao, *Nat. Commun.* **2016**, *7*, 12028.
[22] a) J. Kwon, Y. D. Suh, J. Lee, P. Lee, S. Han, S. Hong, J. Yeo, H. Lee, S. H. Ko, *J. Mater. Chem. C* **2018**, *6*, 7445; b) M. Seong, C. Park, J. Kim, M. Kim, J. Song, H. N. Kim, J. G. Ok, H. E. Jeong, *Mater.Today Nano* **2024**, *27*, 100488.
[23] a) L. Zhang, L. Chen, S. Wang, S. Wang, D. Wang, L. Yu, X. Xu, H. Liu, C. Chen, *Nat. Commun.* **2024**, *15*, 3859; b) S. Yang, J. Cheng, J. Shang, C. Hang, J. Qi, L. Zhong, Q. Rao, L. He, C. Liu, L. Ding, M. Zhang, S. Chakrabarty, X. Jiang, *Nat. Commun.* **2023**, *14*, 6494; c) J. H. Shin, J. Y. Choi, K. June, H. Choi, T.-I. Kim, *Adv. Mater.* **2024**, *36*, 2313157; d) L. Pan, P. Cai, L. Mei, Y. Cheng, Y. Zeng, M. Wang, T. Wang, Y. Jiang, B. Ji, D. Li, X. Chen, *Adv. Mater.* **2020**, *32*, 2003723; e) Y. Zheng, M. Wu, M. Duan, Q. Jin, S. Chen, X. Wang, D. Zhou, *Chem. Eng. J.* **2024**, *488*, 150459; f) L. Zhang, S. Wang, Z. Wang, Z. Huang, P. Sun, F. Dong, H. Liu, D. Wang, X. Xu, *Mater. Horiz.* **2023**, *10*, 2271; g) L. Zhang, S. Wang, Z. Wang, Z. Liu, X. Xu, H. Liu, D. Wang, Z. Tian, *ACS Nano* **2023**, *17*, 13948; h) W. Niu, Q. Tian, Z. Liu, X. Liu, *Adv. Mater.* **2023**, *35*, 2304157.
[24] A. R. Moritz, F. C. Henriques, *Am. J. Pathol.* **1947**, *23*, 695.
[25] Y. Liu, K. Gall, M. L. Dunn, P. McCluskey, *Mech. Mater.* **2004**, *36*, 929.
[26] a) Y. Y. C. Choong, S. Maleksaeedi, H. Eng, S. Yu, J. Wei, P. C. Su, *Appl. Mater. Today* **2020**, *18*, 100515; b) V. Sessini, D. Brox, A. J. López, A. Ureña, L. Peponi, *Nanocomposites* **2018**, *4*, 19.
[27] D. Hwang, C. Lee, X. Yang, J. M. Pérez-González, J. Finnegan, B. Lee, E. J. Markvicka, R. Long, M. D. Bartlett, *Nat. Mater.* **2023**, *22*, 1030.
[28] a) C. B. Haverkamp, D. Hwang, C. Lee, M. D. Bartlett, *Soft Matter* **2021**, *17*, 1731; b) Q. Li, X. Wan, Z. Xu, Y. He, Q. Xue, C. Yang, *Extreme Mech. Lett.* **2024**, *67*, 102128.
[29] P. G. Agache, C. Monneur, J. L. Leveque, J. De Rigal, *Arch. Dermatol. Res.* **1980**, *269*, 221.
[30] Y. Zhai, S. Wu, Q. Hu, W. Zhou, Y. Shen, X. Yan, Y. Ma, *Sci. Rep.* **2023**, *13*, 21416.
[31] D.-H. Kim, N. Lu, R. Ma, Y.-S. Kim, R.-H. Kim, S. Wang, J. Wu, S. M. Won, H. Tao, A. Islam, K. J. Yu, T.-I. Kim, R. Chowdhury, M. Ying, L. Xu, M. Li, H.-J. Chung, H. Keum, M. McCormick, P. Liu, Y.-W. Zhang, F. G. Omenetto, Y. Huang, T. Coleman, J. A. Rogers, *Science* **2011**, *333*, 838.